Replica Exchange Molecular Dynamics Simulation of Organic Matter Evolution: From Lignin to Overmature Type III Kerogen

Jean-Marc Leyssale, Pierre-Louis Valdenaire, Kévin Potier, Roland JM Pellenq

energy&fuels

pubs.acs.org/EF

Article

Replica Exchange Molecular Dynamics Simulation of Organic Matter Evolution: From Lignin to Overmature Type III Kerogen

Jean-Marc Leyssale,* Pierre-Louis Valdenaire, Kévin Potier, and Roland J.-M. Pellenq

Cite This: *Energy Fuels* 2022, 36, 14723−14733

Read Online

ACCESS | Metrics & More | Article Recommendations

ABSTRACT: Much more than any other form of carbon, kerogen undergoes considerable chemical and structural evolution during natural maturation. Some properties, such as gas adsorption and transport capacity, which are very important for key energy and environmental issues in the context of shale hydrocarbon recovery or CO_2 sequestration, may therefore depend significantly on maturity. Here, we report on an extension of a recent work by Atmani et al. [*Energy Fuels***2020**, *34*, 1537−1547] in which we use the replica exchange molecular dynamics method to investigate the natural evolution of a softwood lignin model up to a largely overmature state with H/C = 0.13. We discuss in details the production of a fluid during the process and the evolution of the kerogen texture, structure, and properties via a detailed analysis of nine kerogen models of increasing maturity. We show that the kerogen is composed of small aromatics, branched by aliphatic chains, and is mostly nonporous in its immature state. It becomes increasingly aromatic during evolution, up to creating a percolating ring network at the overmature stage, while progressively increasing in porosity. In the final state, the overmature kerogen is highly porous, and the results suggest the presence of mesopores, even though the latter could not be captured due to the limited size of the simulation cell. The series of type III kerogen models produced in this work, with maturity ranging from immature to overmature, can be used in future work to investigate gas adsorption and transport properties.

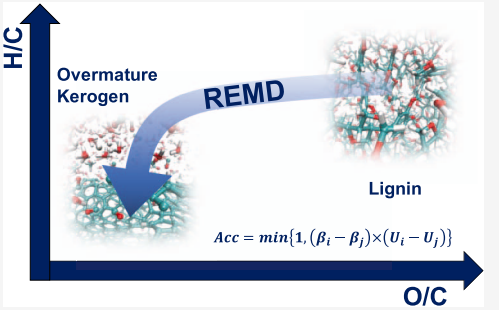

INTRODUCTION

Despite being by far the most abundant form of carbon on Earth, the structure and properties of kerogen[1] are less well investigated than those of other forms of natural carbon, like coal or graphite. However, the sudden development of unconventional fuels in the early 2000s[2−4] has marked a significant regain of interest for this fossil carbonaceous solid, which encloses most of the targeted gas/oil within its porosity in so-called shale deposits. While the nature of the minerals, accounting for more than 90% of the mass in shale,[5] is obviously important regarding the efficiency of the hydro-fracking process in recovering oil and gas, kerogen is thought to play an essential role. Hydrocarbons are so tightly adsorbed within the kerogen matrix that it is generally assumed that a vast majority (more than 90% in some cases[6,7]) of the hydrocarbons are not recovered due to the low permeability of the kerogen in common shale plays. This has motivated a considerable amount of interest in the properties of kerogen over the past two decades.[8−11]

Although in some countries, unconventional gas and oil are still considered acceptable alternatives to more polluting energy resources (i.e., coal),[3] climate change is leading many decision-making actors to move away from fossil fuels. Nevertheless, there still exist some greener perspectives for unconventional fuels, and especially those based on enhanced gas recovery via high-pressure CO_2 injection, which would ensure natural gas supply at low environmental impact via long-term sequestration of CO_2 in a coalbed or kerogen.[6,12−14]

Investigating kerogen properties, especially gas adsorption, transport, and mechanical properties, requires separating kerogen from the minerals in shale, which is achieved through complex and aggressive chemical treatments.[15] Furthermore, such demineralization is often incomplete, contaminating some characterization data with intense signals from mineral impurities, as in the case of X-ray diffraction.[16] Also, kerogen may present a wide range of compositions and textures, depending on the parent organic matter (OM) and burial history.[1] Obtained samples may thus be heterogeneous. Oil and gas-prone kerogen is usually classified into three main categories, depending on the sedimentary environment, which differ in their evolution (or maturation) pathways on the van Krevelen diagram.[17] Type I kerogen is from lacustrine environments and has the largest H/C and lowest O/C content. Type III kerogen arises from terrestrial deposits and

Received: September 4, 2022
Revised: November 8, 2022
Published: November 21, 2022

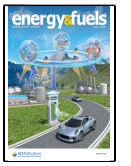

has the lowest H/C and largest O/C content, while type II kerogen, from marine deposits, shows an intermediate evolution pathway. During evolution, kerogen produces fluid (water, carbon monoxide, and dioxide as well as hydrocarbons) while losing most of its H and O contents (as well as other heteroelements like sulfur and nitrogen). Meanwhile, the kerogen structure evolves from a branched polymeric macromolecular compound to an aromatic carbon.[1]

Molecular simulations have shown great capacity to complement analytical research as well-defined microstructures can be prescribed in simulations. Thermodynamic,[18] mechanical[16,19] as well as gas adsorption[20] and transport[21,22] properties of kerogen have been investigated using molecular simulations. Central to all of these studies is the use of three-dimensional (3D) atomistic representations of the kerogen microstructures, with the most widely used so far being those of Ungerer et al.[18] Following earlier works by Béhar and Vandenbroucke[23,24] and Siskin et al.,[25] Ungerer et al.[18] proposed a series of digital kerogen molecules that were constructed according to the compositions and chemical functions reported in Kelemen et al.[10] These molecules can be packed together via molecular dynamics (MD) simulations to create bulk kerogen models of various types and maturities.

Bousige et al.[16] proposed atomistic models of four different samples by a reconstruction technique, the hybrid reverse Monte Carlo (HRMC) method, aiming at reproducing pair distribution functions derived from diffraction experiments. Although less accurate than the "molecular" models, from the point of view of chemical functionalization, Bousige's models form 3D-connected periodic models, which more accurately account for porosity and mechanical properties than the "molecular" models, which are all based on relatively small molecules with a mass of about $(2-3) \times 10^3$ g/mol only.

More recently, Atmani et al.[26] proposed an original approach based on the replica exchange molecular dynamics (REMD) simulation technique, coupled with reactive molecular dynamics (RMD), that allow simulating the evolution of OM under the temperature and pressure of kerogen formations. While RMD is often used to simulate organic matter pyrolysis,[27,28,30−37] the limitation of RMD simulations to time scales well below the millisecond requires performing the simulations at high temperatures, typically in the 2000−3000 K range, where the thermodynamic conditions are so different from those prevailing in experiments that comparison of results is usually delicate.[27,29] In the REMD method, high temperatures are also used to accelerate chemical reactivity, yet the same system is run in parallel at many temperatures, from the one of interest (typically the one relevant to kerogen maturation) up to a maximum temperature at which chemical reactions take place within a ps time scale. Then, during the simulation, an exchange mechanism operates between replicas operating at close-by temperatures, ensuring that all replicas are driven to their own equilibrium states. Using REMD, Atmani et al. simulated the geological evolution of cellulose[26] and lignin,[38] two important constituents of type III OM, up to mature kerogen (atomic H/C ∼ 0.5), unraveling unprecedented details on kerogen formation and evolution mechanisms, as well as on the nature and quantity of the produced fluid. Here, Atmani et al.'s simulation of lignin evolution is significantly extended, from 1.3 ns of REMD time in ref 38 to 7 ns, allowing one to capture most of the metagenesis stage (H/C < 0.5). We describe in what follows the details on the fluid production and kerogen property evolution up to a highly overmature stage with H/C = 0.13. We add that in the maturity domain considered here, typical of metagenesis, all kerogen types show very similar behavior, albeit differing in texture.[1] Therefore, most of the presented results, excluding discussions on texture, apply to kerogen in general, whatever its origin. Note that metagenesis is the last stage of kerogen maturation. It corresponds to the conversion of organic matter to dry gas, mostly. Metagenesis occurs at temperatures in the range of 423−473 K.

COMPUTATIONAL METHODS

The calculations presented in this work are the continuation of the work presented recently in Atmani et al.;[38] the methods are essentially the same. We briefly recall here the main elements. The thermal maturation of lignin was investigated with REMD using a lignin model constructed by equilibrating an assembly of 18 prototype molecules of softwood lignin, with the composition $C_{90}H_{100}O_{31}$, proposed by Crestini et al.[39] These molecules were inserted in a large orthorhombic box with periodic boundary conditions and then compressed at 25 MPa and 423 K using MD in the NPT ensemble for about 100 ps. The equilibrated system was then subjected to REMD for 1300 ps. In this simulation, 96 replicas of the system were simulated in parallel in the canonical ensemble at the same composition (number of atoms N), volume (V), and increasing temperature (T) from 423 K, for replica 1, to 3500 K for replica 96, with exponential temperature spacing. At regular intervals, attempts to exchange the configurations of adjacent replicas were performed and accepted or rejected with the canonical acceptance criterion,[40,41] ensuring that each replica is driven toward its underlying canonical distribution. Doing so, the evolution of the system at the temperature of interest is considerably accelerated, and one can observe the conversion of OM into kerogen within a few hundreds of ps (REMD time), against millions of years in nature. More precisely, REMD trajectories can be seen as a succession of metastable states of decreasing Helmholtz free energy in the path to equilibrium,[42] yet there is no guarantee that the true thermodynamic equilibrium is reached.

An important limitation in REMD simulations is that the constraint of working at constant volume leads to unrealistic pressure development, up to a few hundred MPa, in the system because of fluid production during maturation. This issue was dealt with by interrupting the REMD process every 200 ps, relaxing the 423 K replica at the target pressure (using 100 ps NPT runs), and then, the REMD process was relaunched with all of the replicas reinitiated with the configuration of the relaxed 423 K replica.[38] Using this strategy, we observed the evolution of the kerogen up to a relatively high maturity level with atomic H/C and O/C ratios of about 0.5 and 0.02, respectively (compared to 1.11 and 0.34 for lignin). Yet, after a few hundred ps, the system showed no more evolution. Especially, the metagenesis step, where a clear increase in the rate of H/C vs O/C evolution in the van Krevelen diagram is expected,[1] was not observed in the simulation. These results clearly indicate a slowdown in the evolution kinetics near metagenesis. However, the regular reinitialization of the REMD process due to the pressure relaxation steps may hinder the evolution of the system in a stage where evolution kinetics is slow compared to the frequency of pressure relaxation steps. In this work, we present results of the continuation of the REMD simulation for an additional 5.7 ns, compared to the 1.3 ns previously investigated.[38] Also, to facilitate the system's evolution, pressure relaxation was omitted, meaning that the REMD process is uninterrupted during the whole 5.7 ns. This will lead to a substantial pressure increase, yet we assume that this is of marginal effect.

Interatomic interactions are described by the ReaxFF forcefield.[43] More precisely, we use the Atmani et al. parameterization,[26] which contains the C−C parameters from the Reax2013 parameterization,[44] the C−H parameters from Shin et al.,[45] and the C−O parameters trained from an extended database.[42] In addition to the work described above,[38] this forcefield was also used to investigate the

https://doi.org/10.1021/acs.energyfuels.2c02963
Energy Fuels 2022, 36, 14723−14733

kinetics of the dehydration of cellulose,[46] the natural evolution of cellulose,[26] and the carbon nucleation from deep hydrothermal fluids.[42] The MD and REMD simulations are performed using the large-scale atomic/molecular massively parallel simulator (LAMMPS) package.[47] They use the velocity-Verlet integrator,[48] with a 0.1 fs ep, a Nosé−Hoover thermostat, and a Nosé−Hoover−Andersen barostat (NPT only) as implemented by Shinoda et al.[49] Time constants for the thermostat and barostat are 50 and 500 fs, respectively. Replica exchange moves are attempted every 10 fs, and the success rate is about 20%.

Atomic configurations of the different replicas are stored at intervals for analysis. In this work, we only consider for analysis the configurations stored for the replica at 423 K (the temperature of geological interest), at different REMD times. First, individual molecules are determined using a standard clustering algorithm based on bond cutoffs, with the usual values of 1.9 Å for C−C, C−O, and O−O bonds, 1.5 Å for C−H bonds, 1.35 Å for O−H bonds, and 1.1 Å for H−H bonds.[26] This allows for the classification into four categories depending on the number of atoms in the molecule: gas up to 4 C atoms, light tar (oil) from 5 to 13 C atoms, heavy tar from 14 to 40 atoms, and kerogen for more than 40 atoms.[50]

Finally, the kerogen models are relaxed for 5 ns at 423 K and 25 MPa using MD in the NPT ensemble. Only the last 3 ns are considered for the calculation of properties. A unique configuration of each kerogen model is used to compute properties that do not fluctuate during relaxation. It includes the H/C and O/C atomic ratios, the C atom coordination statistics, and the ring statistics, characterizing the medium-range order, and which are identified using the shortest path ring algorithm[51] implemented in an in-house code. Following the identification of rings, ring clusters, defined as an assembly of rings sharing a common bond, are identified, as well as chain fragments, defined as bonded clusters of atoms that do not belong to rings. Statistics on ring and chain cluster sizes are also computed. Only C and O atoms are considered for these analyses.

The probeless porosity was computed by sampling the matrix using a grid of 0.1 Å lattice spacing and determining the fraction of the volume that does not overlap with matrix atoms. Diameters of 3.36, 3.17, and 2.42 Å were adopted for C, O, and H atoms, respectively. Pore size distributions were determined by computing, for every grid point in the porosity, the largest spherical pore to which it can belong. These analyses were performed using an in-house code,[38] adapted to the probeless case (i.e., equivalent to a probe of radius equal to zero). For these calculations, six independent configurations, distant by 500 ps, are used.

X-ray diffraction patterns are computed from single configurations using the Debye equation:

$$I(Q) = \sum_i \sum_j f_i f_j \frac{\sin(Qr_{ij})}{Qr_{ij}} \quad (1)$$

where I is the scattered intensity, Q is the scattering vector, f_i and f_j are the atomic scattering factors of atoms i and j, respectively, and r_{ij} is the interatomic distance. The calculations are performed with Debyer software[52] with appropriate cutoff corrections and accounting for periodic boundary conditions. Scattering vectors are converted to diffraction angles, 2θ, according to $Q = 4\pi \sin\theta/\lambda$, adopting λ = 0.1542 nm (Cu Kα).

Finally, the volumetric properties (density and bulk modulus) are computed using the last 3 ns of the relaxation simulations. The bulk moduli K are computed from the fluctuations of the volume according to $\frac{1}{K} = \frac{\langle V^2\rangle - \langle V\rangle^2}{k_B T\langle V\rangle}$, where k_B is Boltzmann's constant and $\langle\cdots\rangle$ indicate time averages. Values are given as the mean and standard deviation (error bar) on the mean using block averaging with four blocks of 750 ps.

Unless explicitly stated, all of the presented results refer to the replica of geological interest, namely, the 423 K replica.

RESULTS

Unless explicitly stated, all of the presented results refer to the replica of geological interest, namely, the 423 K replica. Figure 1 shows the evolution of the potential energy (U_P), pressure (P), and volume (V) of the system during the REMD simulation. The evolution of the system is clearly driven by a decrease in potential energy during the whole simulation, even though this reduction is greater during the early stage of the simulation. We also observe that the constraint of performing the simulation at constant volume, starting from 1.3 ns, leads to a rather significant increase in the system pressure: P increases from about 25 MPa at 1.3 ns to about 350 MPa after 7 ns. Although somehow unrealistic, we assume that this level of pressure should not significantly affect the chemical respeciation of the system. Previous works show, in any case, that it did not affect the structure of the kerogen.[53,54] Furthermore, under these high-pressure, temperature, and confinement conditions, all fluids are in a supercritical state.[55] Therefore, increasing P from 50 to 350 MPa would only increase the bulk density of water by about 15% and of the other fluids by about a factor 2. Hence, this would not have much effect on the reaction kinetics (irrelevant to this work) and thermodynamics. The increase in pressure, or confining stress, may also influence the texture of the kerogen, and especially the alignment and organization of the aromatic layers, yet at the investigated scale, no evidence of such an effect is observed (see below). We also note that, even though REMD could be performed in the NPT ensemble, as discussed earlier,[38] constant pressure conditions could trigger gasification of the system in the high-temperature replicas (e.g., 3500 K), hindering the formation and evolution of the kerogen.

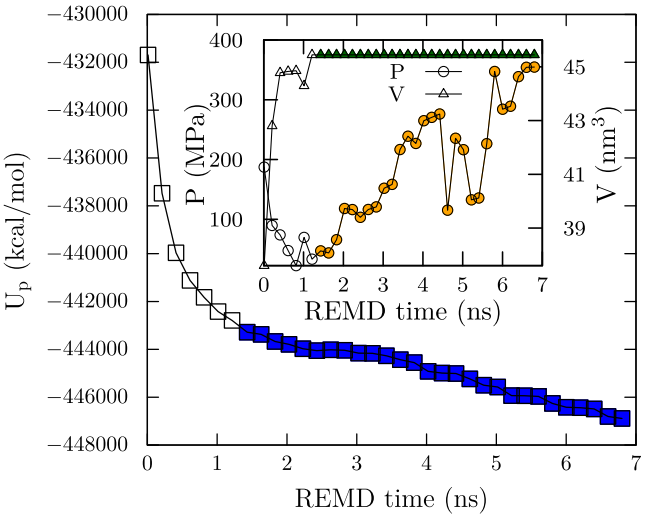

Figure 1. Evolution with REMD time of the main thermodynamic variables for the 423 K replica: potential energy U_P (squares), pressure P (circles, inset), and volume V (triangles, inset). Empty and filled symbols relate to previously published[38] and new results, respectively.

Figure 2 shows the evolution of the mass fractions of gas, light tar, heavy tar, and kerogen during the simulation. As already pointed out,[38] the system evolves very quickly (in a few hundred picoseconds) to a stage at which it is composed of about 41%, in mass, gas and 58% kerogen. These ratios remain constant throughout the rest of the simulation. We recall here that the kerogen yield is within typical values of char yields

https://doi.org/10.1021/acs.energyfuels.2c02963
Energy Fuels 2022, 36, 14723−14733

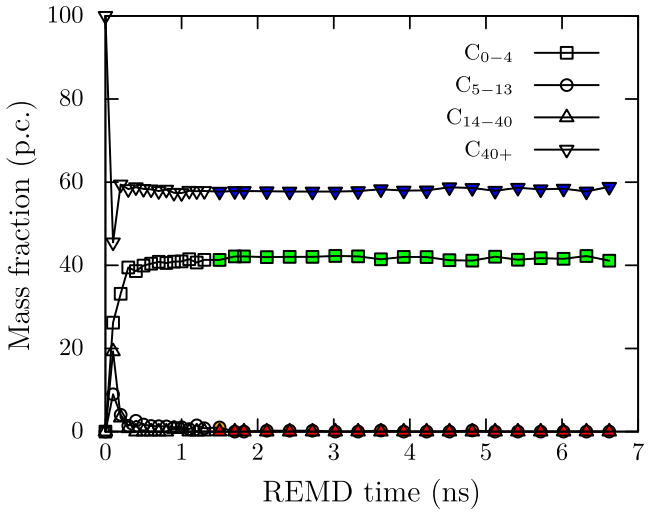

Figure 2. Evolution with REMD time of the mass distribution in the 423 K replica: gas (squares), light tar (circles), heavy tar (up triangles), and kerogen (down triangles). Empty and filled symbols relate to previously published[38] and new results, respectively.

observed after lignin pyrolysis experiments, showing values of 40−69% depending on the pyrolysis temperature and time.[56,57]

While the average kerogen and gas yields remain constant, some respeciation necessarily takes place within the gas and/or kerogen to account for the change in U_P and P observed in the last 6 ns of simulation (see Figure 1). As can be seen in Figure 3, after an important production in the early stages, the

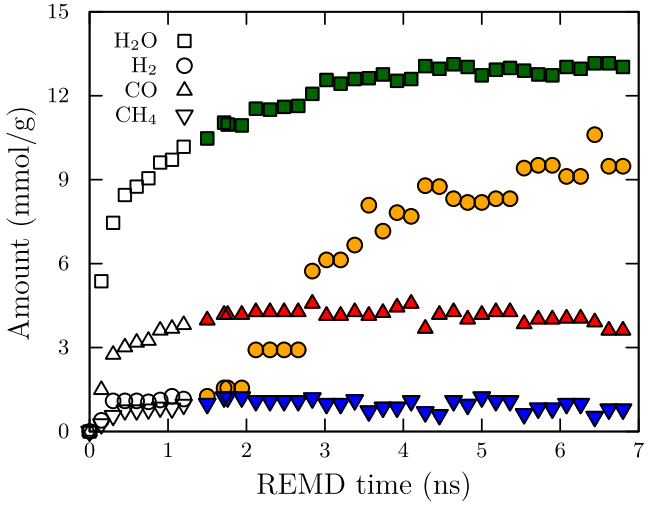

Figure 3. Evolution with REMD time of the main produced fluid molecules for the 423 K replica: water (squares), hydrogen (circles), carbon monoxide (up triangles), and methane (down triangles). Empty and filled symbols relate to previously published[38] and new results, respectively. Yields are given in units of mmol of fluid per gram of lignin.

amounts of methane and carbon monoxide plateau at about 1 and 4 mmol/g, respectively, and slightly decrease during the rest of the simulation. Conversely, water production continually increases, reaching a plateau of about 13 mmol/g at about 4.5 ns. As expected for a mature kerogen, we also observe a significant increase in hydrogen production between 2 and 7 ns of REMD simulation, up to about 10 mmol/g.

The increase in water and hydrogen is necessarily associated with the release of O and H atoms from the kerogen and, hence, with its maturation. As shown in Figure 4, the O/C

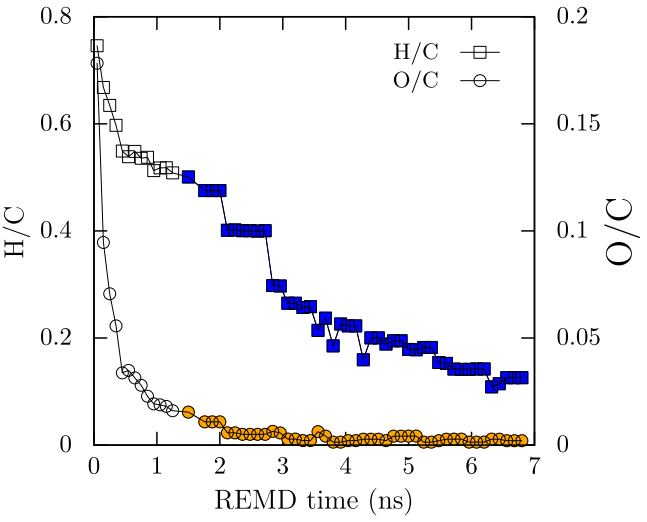

Figure 4. Evolution with REMD time of the solid atomic H/C (squares) and O/C (circles) ratios for the 423 K replica. Empty and filled symbols relate to previously published[38] and new results, respectively.

ratio in the kerogen quickly decreases to very low values, reaching a plateau of about 0.0024 at the water yield plateau (i.e., for REMD times larger than 4.5 ns). The H/C ratio also decreases during the simulation, yet at a much slower pace, reaching about 0.125 after 7 ns.

This difference in O and H loss during kerogen evolution is well-known and better illustrated by plotting the evolution of H/C as a function of O/C in the van Krevelen diagram.[1,17] As shown in Figure 5, an evolution typical of type III kerogen is recovered and a significant decrease in H/C when O/C only marginally diminishes, common to all kerogen types in the late

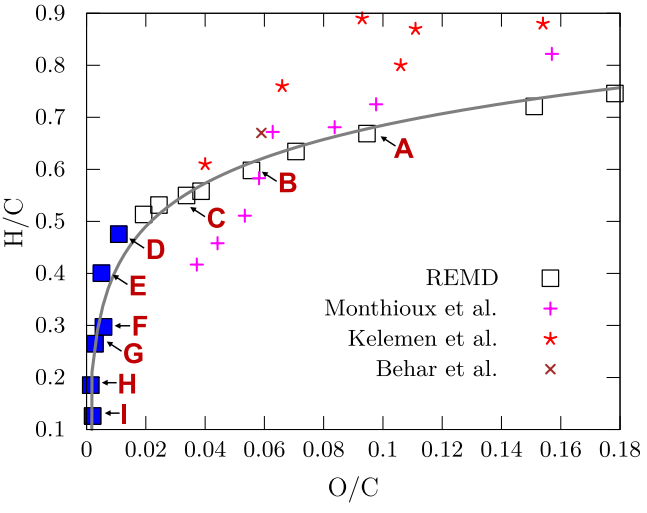

Figure 5. Van Krevelen plot (H/C *vs* O/C) of kerogen evolution. Empty and filled symbols relate to previously published[38] and new results, respectively. Data on type III OM pyrolysis experiments from Monthioux et al.[58] and natural type III kerogen from Kelemen et al.[10] and from Béhar et al.[23] are shown for comparison. The gray line is a power law fit to the data, serving as a guide to the eye.

https://doi.org/10.1021/acs.energyfuels.2c02963
Energy Fuels 2022, 36, 14723−14733

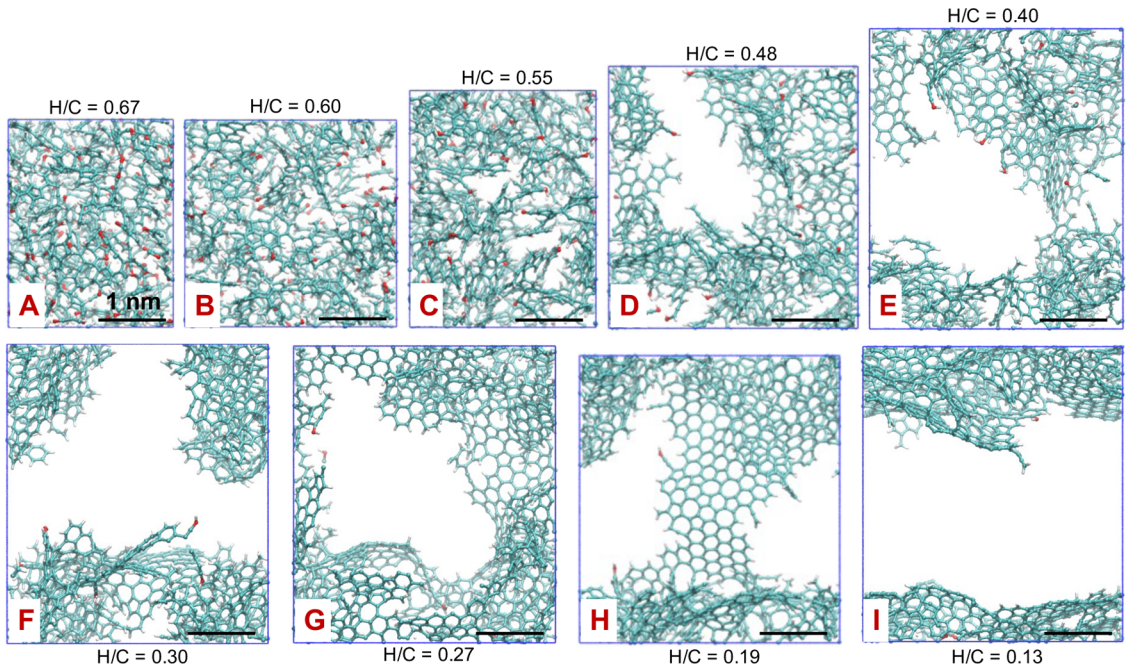

Figure 6. Snapshots of the kerogen models at different maturities (H/C ratios). The color code reads as follows: cyan, C; red, O; and white, H. Models F and I only show periodicity in the two horizontal directions; the dimension along the vertical axis is arbitrary for these two models.

(metagenesis) evolution stage, is also observed. In earlier stages, REMD data are found within known experimental data for the type III kerogen, from Béhar et al.[23] and Kelemen et al.,[10] as well as the data on type III kerogen pyrolysis observations by Monthioux et al.[58]

We now describe in detail the structural and textural properties of a series of nine kerogen models marked with red uppercase characters, from A to I, in Figure 5. We will use the H/C ratio as the main metric for maturity, knowing that (i) H/C and O/C have related evolutions, with the one of H/C being smoother; and (ii) H/C is more related to the texture evolution (especially the aliphatic/aromatic ratio), while O/C is more about functionalization of surface groups. Prior to the analysis, all fluid molecules were removed from the kerogens' porosity and the models were relaxed at 423 K and 25 MPa using MD in the NPT ensemble. We acknowledge that at 423 K, pressure should rather be in the 50 and 125 MPa ranges, corresponding to the hydrostatic and lithostatic limits, respectively, for a depth of ∼5 km. We adopted the value of 25 MPa (which corresponds to the typical hydrostatic pressure at 3 km depth) to be consistent with previous investigations[26,38] in which this pressure was chosen to compensate for the increase in pressure during the REMD simulations. Snapshots of the nine relaxed kerogen models are shown in Figure 6. As can be seen, significant evolution in the kerogen takes place during maturation. While H/C decreases from 0.67 to 0.13, a significant decrease in density and increase in porosity can be observed. In addition to the obvious decrease in O/C, there is a progressive development of aromaticity (Figure 6). At the scale of these simulations, we also observe that two of the models (F and I) are no more 3D-connected but instead form two-dimensional (2D) membranes along the horizontal directions. For this reason, these two models would have unrealistic mechanical properties in the z direction; hence, NPT relaxation was only performed in the x and y directions for these two models.

The evolution of the C atoms' coordination numbers is given in Figure 7. Throughout the simulation, the amount of

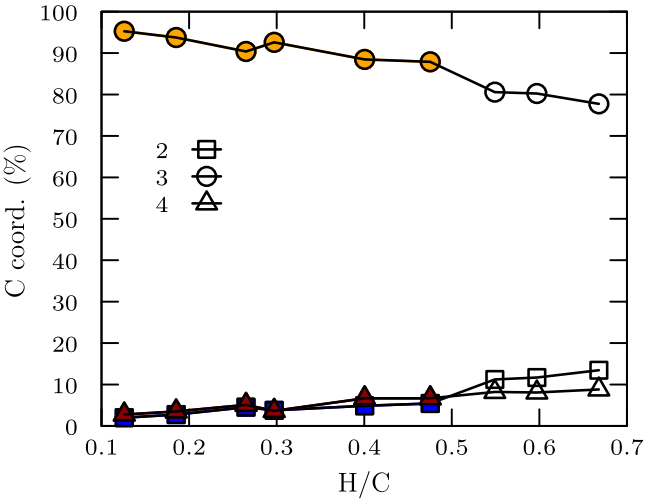

Figure 7. Evolution with maturity (H/C ratio) of the coordination fractions of the C atoms: squares (2, sp or radical sp^2), circles (3, sp^2), and triangles (4, sp^3). Empty and filled symbols relate to previously published[38] and new results, respectively.

three-coordinated atoms (sp^2 hybridization) increases from about 78% for model A (H/C = 0.67) to about 95% for model I (H/C = 0.13). Meanwhile, the fractions of two-coordinated (sp and sp^2 radicals) and four-coordinated (sp^3) atoms decrease from 13 to 2% and from 9 to 3%, respectively.

Figure 8 shows the evolution of some textural parameters with the H/C ratio: the ratio of heavy atoms (C and O) in rings and chains (Figure 8a) and the size in atoms of ring clusters (Figure 8b) and of chain clusters (Figure 8c). During evolution, we see that the ring/chain ratio increases from about 1.3 for model A to about 25 for model I, indicating a

https://doi.org/10.1021/acs.energyfuels.2c02963
Energy Fuels 2022, 36, 14723−14733

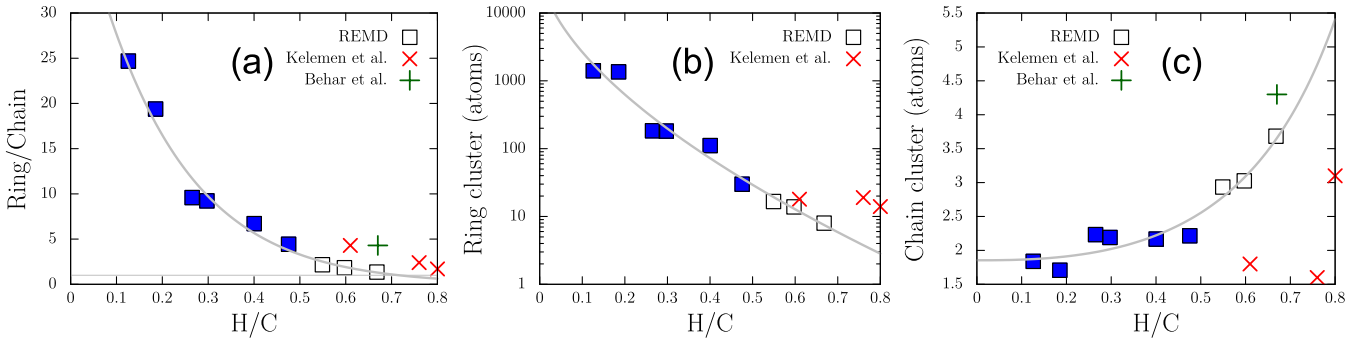

Figure 8. Evolution with maturity (H/C ratio) of the textural parameters: (a) ratio of heavy atoms (O and C) in the ring and chain structures; (b) average size of ring clusters; and (c) average size of chain clusters. Empty and filled squares relate to previously published[38] and new results, respectively. Crosses, experimental data from (+) Behar et al.[23] and (×) Kelemen et al.[10] Gray lines are stretched exponential fits to data, serving as guides to the eye.

pronounced aromatization of the kerogen (Figure 8a). Meanwhile, the average size of ring clusters (Figure 8b) increases from about 8 atoms (1−2 rings) to about 1400 atoms (~600 rings). Conversely, the average size of chain clusters (Figure 8c) decreases from about 3.7 to 1.8 atoms. These quantities can be compared, at least semiquantitatively,[38] to the ratio of aromatic over aliphatic carbon and the size of aromatic and aliphatic clusters determined from NMR data for a few type III kerogen samples by Béhar et al.[23] and Kelemen et al.[10] Even though experimental data only exist for relatively large H/C values (≥0.6), and appear relatively scattered, their numerical values are compatible with the REMD results for lignin evolution.

Figure 9 shows the evolution of the ring statistics in the kerogen. Throughout the evolution, the ring structure is

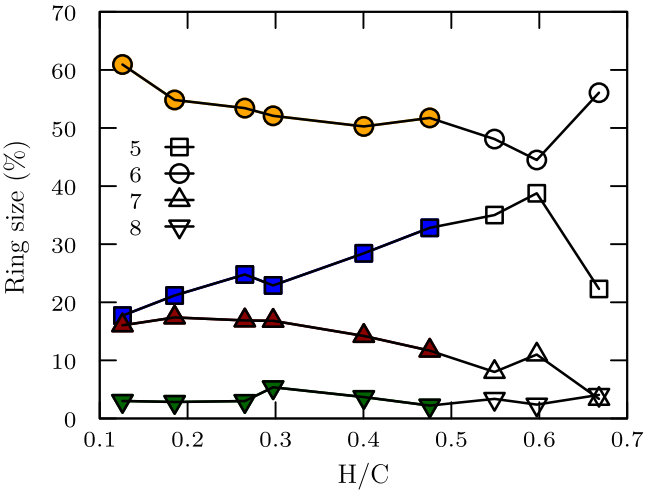

Figure 9. Evolution with maturity (H/C ratio) of the ring size statistics: squares, pentagons; circles, hexagons; up triangles, heptagons; down triangles, octagons. Empty and filled symbols relate to previously published (ref 38) and new results, respectively.

dominated by hexagons, representing between 44 and 61% of the rings in the kerogen. Albeit some fluctuations, the fraction of hexagonal rings increases with maturity, indicating a tendency toward graphitization. Not considering model A (H/C = 0.67), which somehow appears as an outlier in the statistics, maybe because of a lower number of rings, we see that the fraction of pentagons decreases with maturity, from about 38 to 18% from model B (H/C = 0.6) to model I (H/C = 0.13). Conversely, the fraction of heptagonal rings increases from about 3 to 7%, while the fraction of octagons remains fairly constant and at a much lower value (~3−4%). The ratio of pentagons to heptagons is highly correlated with the curvature of the carbon structure.[42] When this ratio is larger than unity, isolated pentagons induce a positive curvature (fullerene-like) of the carbon layers,[59] which is the case in the earlier stage of kerogen evolution. For low H/C values, typically <0.3, this ratio gets close to unity and the carbon layers adopt more planar structures due to the formation of pentagon/heptagon pairs.[60,61]

Figure 10 shows the computed X-ray diffraction patterns of the kerogen models. For all models, the signal is very broad,

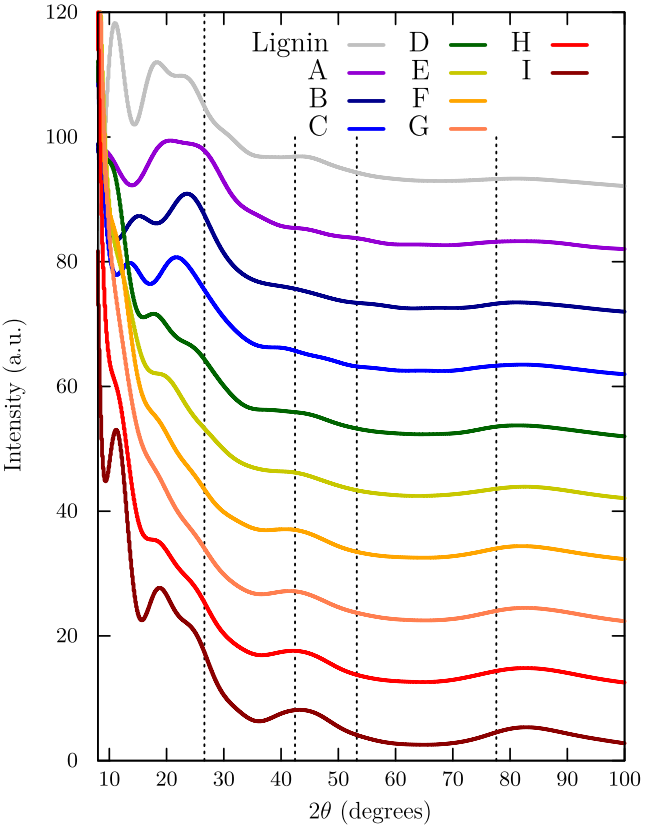

Figure 10. X-ray diffraction patterns of the kerogen models. Thin dashed vertical lines indicate the locations of the 002, 100, 004, and 110 peaks in graphite, by increasing value of 2θ.

https://doi.org/10.1021/acs.energyfuels.2c02963
Energy Fuels 2022, 36, 14723−14733

which is indicative of a mostly amorphous structure. Yet, one can observe some peaks at low angles (<30°) for the models in the early evolution stages, which probably represent some remains of the parent lignin structure (see the pattern of lignin on top of Figure 10). At higher maturity, some broad bands, typical of turbostratic carbons, become visible around the theoretical locations of graphite's 100 and 110 peaks, at 42 and 78°, respectively. Some bump on the baseline is also visible at angles slightly below the theoretical 002 angles (27°), indicating some turbostratic layer stacking.[62] Interestingly, the patterns obtained for mature kerogen closely resemble those measured for nongraphitizing saccharose-based chars heat-treated in the 400−1000 °C range[63] and for which atomistic models were produced using the HRMC technique.[64]

To further evaluate the diffraction data, we show in Figure 11 a close-up of the diffraction pattern of model I (the most mature) around the 2θ domain area of graphite's 100 and 004 peaks after removal of the baseline. The signal is well-fitted with the two usual bands for turbostratic carbon, which are significantly overlapping in such disordered materials. We observe that the in-plane 10 band is almost perfectly located at graphite's 100 peak location, while the pure out-of-plane 004 band is significantly shifted (by about 6 degrees) to lower angles with respect to graphite's 004 peak. Crystalline coherence lengths, L_a = 2.1 nm and L_c = 0.9 nm (~3 stacked layers) for in-plane and out-of-plane orders, respectively, are obtained using the Scherrer−Warren relations: $L_{a,c} = K_{a,c}\lambda/(\beta\cos(\theta))$, where K_a = 1.77, K_c = 1, λ = 1.542 Å, β is the full width at half-maximum of the peak, and θ is the diffraction half-angle. The interlayer distance d_{002} = 3.83 Å is obtained from the 004 peak location (2θ = 47.54°) using Bragg's law.

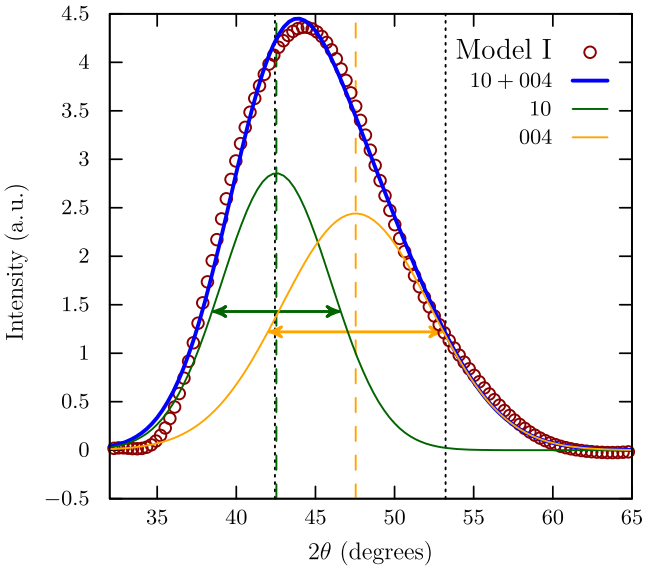

Figure 11. X-ray diffraction pattern of model I around the 10 band/004 peak locations. Circles indicate the computed pattern in Figure 10 after removing the baseline using a power law fit. Two Pearson VII functions with adjustable positions and widths were used to fit the signal. Corresponding peak locations in graphite are indicated with black dotted lines, and the position and width of the 10 and 004 bands are marked with dashed vertical lines and horizontal arrows, respectively (10: green; 004: orange).

We show in Figure 12 the evolution with maturity of some physical properties, namely, the density, porosity, and bulk modulus. Starting at a value of ~1.3 g/cm^3 at H/C = 0.67, the density decreases by almost a factor of 2 for H/C ≤ 0.4, where it somehow remains constant (Figure 12a). This decrease in density is clearly associated with the volume expansion observed in the early stage of simulation (see Figure 6) and porosity development (Figure 12b) induced by the fluid production (Figure 3). Interestingly, as pointed out in ref,[38] and conversely to what was observed for cellulose,[26] the kerogen formed from lignin burial remains rigid enough to conserve most of its porosity after fluid expulsion starting from moderate maturity (i.e., H/C ~ 0.55).

As can be seen in Figure 12c, the bulk modulus K did not show a clear evolution with H/C and remained between 0.5 and 3.5 GPa. Nevertheless, we can see a tendency toward a decrease in K with decreasing H/C for H/C ≥ 0.4. Then, a slight increase is visible when H/C further decreases. This evolution in stiffness can be rationalized by the compensation of two opposite effects. At large H/C values, the kerogen is made of many ring clusters that are connected through short chain moieties (see the snapshot of model D in Figure 12d). On decreasing H/C, the density decreases, which in turns lead to a decrease in stiffness.[16] Meanwhile, when H/C decreases, the ring clusters coalesce into larger clusters, yet still not into a percolating one (see model E in Figure 12e) in the vertical direction. Finally, at some critical H/C value (between 0.27 and 0.4), the ring structure coalesces into one main percolating cluster, while the density remains almost constant, explaining the sudden rise in stiffness.

Figure 13 shows the evolution of the pore size distribution of the kerogen during its evolution. In the early stage of the simulation, most of the porosity corresponds to extremely narrow pores, below the molecular diameters of common adsorption probes like N_2, CO_2, or Ar, which are all in the 3−4 Å range. Model A, in particular, can be considered as nonporous with respect to these gases. With increasing maturity, and as observed in Figure 6, porosity starts to appear in the kerogen. Model C, with pore diameters up to ~7 Å, is a typical ultramicroporous carbon, while model D, with a rather flat PSD up to ~17 Å, belongs to the microporous carbon category according to IUPAC.[65] When H/C ≤ 0.4 (models E, G, and H), the PSD extends to about the same maximum pore diameter of ~2 nm, at the edge of the nanopore/mesopore boundary.[65] We even observe that the further the H/C decreases, the more the proportion of large pores becomes important (compare models E and H), indicating pore coalescence during the evolution process. This is a clear indication that mesopores should actually be present in the models in this evolution stage. However, the latter, with pore diameters larger than 2 nm, can obviously not be captured in such small-sized models as those investigated here (orthorhombic boxes of 2−4 nm width). Another indirect proof that mesopores should have developed in the kerogen is the observed loss of 3D connectivity in two of the models (F and E) in these high-maturity states. These results agree well with those obtained with HRMC kerogen models, showing that kerogen presents accessible microporosity, and no mesoporosity, in the 0.8−1.2 g/cm^3 density range.[16,66]

CONCLUSIONS

The evolution of lignin under a typical geological temperature (423 K) was simulated using an extended REMD simulation,

https://doi.org/10.1021/acs.energyfuels.2c02963
Energy Fuels 2022, 36, 14723−14733

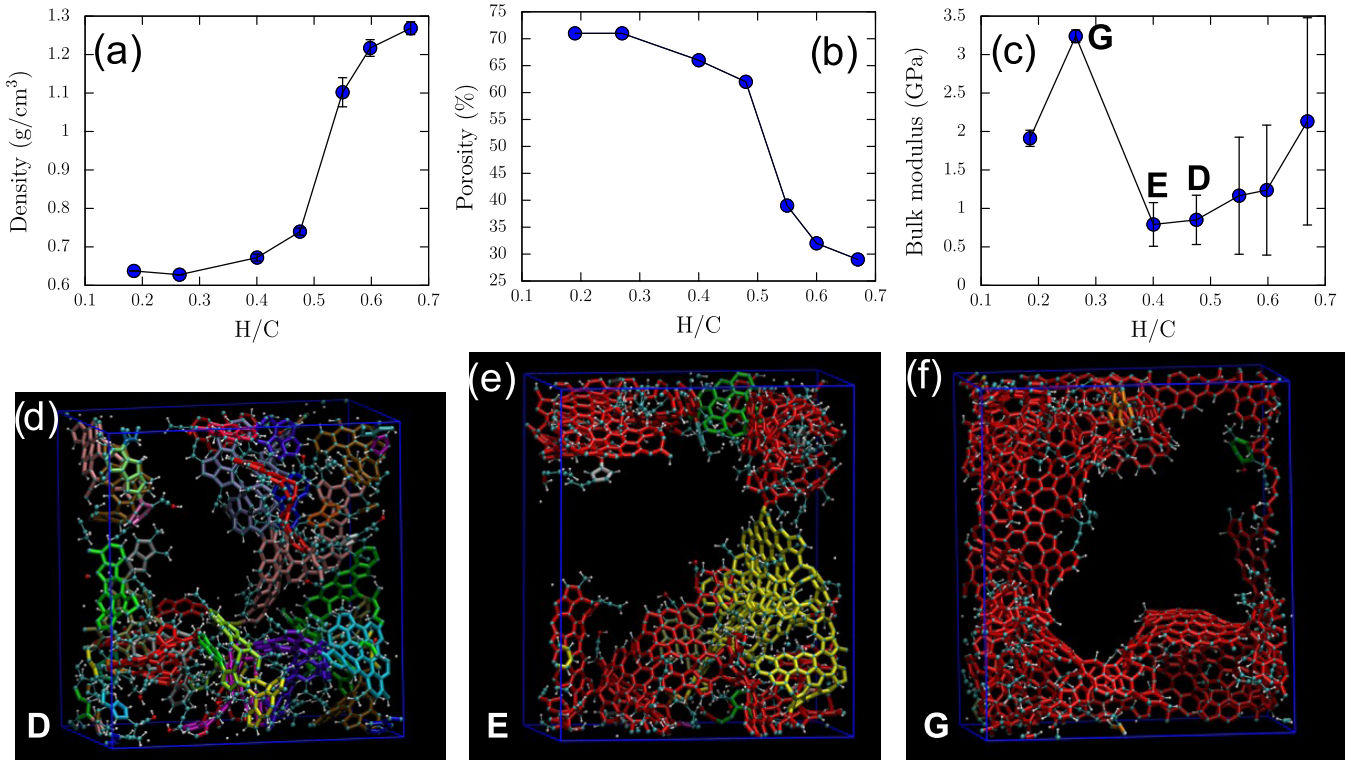

Figure 12. Evolution with maturity of the (a) density, (b) porosity, and (c) bulk modulus of the kerogen. (d–f) Snapshots of models D, E, and G are given with ring clusters highlighted with large colored sticks, with one unique color per cluster. Models F and I, which are not 3D-connected and hence do not show stiffness in the z direction, are not considered here.

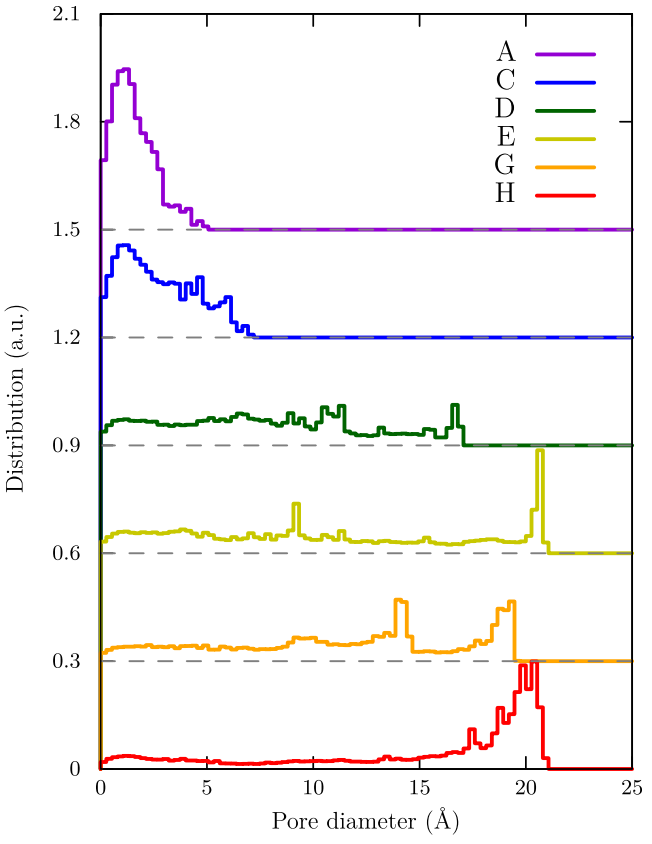

Figure 13. Normalized (probeless) pore size distributions of the 3D-periodic kerogen models.

providing numerous details on the evolution of type III kerogen, despite limitations inherent to the system size and the simplicity of the precursor. It was shown that the lignin polymer quickly decomposes into about 41% gas and 58% kerogen. While the respective masses of gas and kerogen remain almost constant in the rest of the simulation, significant changes occur in the composition of the gas and the composition and properties of the kerogen. Methane and CO contents plateau when the kerogen H/C ratio reaches ~0.5. However, molecular hydrogen and water keep on being produced, while the kerogen further evolves to lower H/C ratios. On releasing hydrogen, the kerogen aromatic content increases with the ring/chain ratio increasing by a factor of 20 from 1.3 at H/C = 0.67 to 25 at H/C = 0.13. When H/C reaches about 0.2, the ring structure percolates into one unique cluster, increasing significantly the stiffness of the kerogen. Meanwhile, the size of chains reduces to about 2 heavy atoms. At this stage, calculation of the diffraction patterns shows graphene domains of ~2 nm with stacks of about 2–3 layers. It was also shown that, nonporous in its more immature form (H/C = 0/67), the kerogen progressively develops porosity during its evolution. Even though not observed because of size limitations, the results even suggest the presence of mesopores for H/C below 0.4. Interestingly, regarding structure, porosity, and stiffness, the most mature kerogen models presented in this work present many similarities to synthetic chars, like the well-known saccharose-derived cokes.[64]

Although one study by Helgeson et al.[67] suggests that kerogen evolution could follow a succession of equilibrium states, driven by the change in overall composition, our work in which composition is fixed rather strengthens the commonly accepted interpretation that kerogen evolution is limited by

https://doi.org/10.1021/acs.energyfuels.2c02963
Energy Fuels 2022, 36, 14723–14733

kinetics, or, in other words, that immature and mature kerogen are metastable intermediates to the formation of graphitic carbon. The final state of the kerogen (i.e., at the end of the 7 ns-long REMD simulation), described above, certainly also constitutes a metastable state that would further evolve toward graphite provided longer simulations are performed.

Finally, the series of kerogen models obtained from the same precursor OM at various maturities constitutes a consistent database of models to investigate maturity effects on properties of interest like gas adsorption and transport.

AUTHOR INFORMATION

Corresponding Author

Jean-Marc Leyssale − *Institut des Sciences Moléculaires, Univ. Bordeaux, CNRS UMR 5255, Talence 33405, France; CNRS/MIT/Aix Marseille Univ. joint lab "MultiScale Materials Science for Energy and Environment", IRL 3466, Massachusetts Institute of Technology, Cambridge, Massachusetts 02139, United States;* orcid.org/0000-0002-7296-922X; Email: jean-marc.leyssale@u-bordeaux.fr

Authors

Pierre-Louis Valdenaire − *CNRS/MIT/Aix Marseille Univ. joint lab "MultiScale Materials Science for Energy and Environment", IRL 3466, Massachusetts Institute of Technology, Cambridge, Massachusetts 02139, United States*

Kévin Potier − *Institut des Sciences Moléculaires, Univ. Bordeaux, CNRS UMR 5255, Talence 33405, France*

Roland J.-M. Pellenq − *CNRS/MIT/Aix Marseille Univ. joint lab "MultiScale Materials Science for Energy and Environment", IRL 3466, Massachusetts Institute of Technology, Cambridge, Massachusetts 02139, United States; EpiDaPo Lab—CNRS/George Washington University, Children's National Medical Center, Children's Research Institute, Washington, District of Columbia 20010, United States*

Complete contact information is available at: https://pubs.acs.org/10.1021/acs.energyfuels.2c02963

Notes

The authors declare no competing financial interest.

[⊥]P.-L.V. recently passed away.

ACKNOWLEDGMENTS

This work was supported by the Game-Changer Shell project enabled through the MIT Energy Initiative and by CNRS and Aix-Marseille University foundation (AMIDEX). It was granted access to the HPC resources of [TGCC/CINES/IDRIS] under the allocation 2016-A0040910065 made by GENCI (Grand Equipement National de Calcul Intensif). Some of the MD simulations presented here were also performed using the facilities of the Mésocentre de Calcul Intensif en Aquitaine (MCIA).

REFERENCES

(1) Vandenbroucke, M.; Largeau, C. Kerogen Origin, Evolution and Structure. *Org. Geochem.* **2007**, *38*, 719−833.

(2) Kerr, R. A. Natural Gas From Shale Bursts Onto the Scene. *Science* **2010**, *328*, 1624−1626.

(3) Sovacool, B. K. Cornucopia or Curse? Reviewing the Costs and Benefits of Shale Gas Hydraulic Fracturing (fracking). *Renewable Sustainable Energy Rev.* **2014**, *37*, 249−264.

(4) Yuan, J.; Luo, D.; Feng, L. A Review of the Technical and Economic Evaluation Techniques for Shale Gas Development. *Appl. Energy* **2015**, *148*, 49−65.

(5) Hackley, P. C.; Cardott, B. J. Application of Organic Petrography in North American Shale Petroleum Systems: A Review. *Int. J. Coal Geol.* **2016**, *163*, 8−51.

(6) Jia, B.; Tsau, J.-S.; Barati, R. A Review of the Current Progress of CO_2 Injection EOR and Carbon Storage in Shale Oil Reservoirs. *Fuel* **2019**, *236*, 404−427.

(7) Mukhina, E.; Cheremisin, A.; Khakimova, L.; Garipova, A.; Dvoretskaya, E.; Zvada, M.; Kalacheva, D.; Prochukhan, K.; Kasyanenko, A.; Cheremisin, A. Enhanced Oil Recovery Method Selection for Shale Oil Based on Numerical Simulations. *ACS Omega* **2021**, *6*, 23731−23741.

(8) Song, J.; Peng, P.; Huang, W. Black Carbon and Kerogen in Soils and Sediments. 1. Quantification and Characterization. *Environ. Sci. Technol.* **2002**, *36*, 3960−3967.

(9) Jarvie, D. M.; Hill, R. J.; Ruble, T. E.; Pollastro, R. M. Unconventional Shale-Gas Systems: The Mississippian Barnett Shale of North-Central Texas as One Model for Thermogenic Shale-Gas Assessment. *AAPG Bull.* **2007**, *91*, 475−499.

(10) Kelemen, S. R.; Afeworki, M.; Gorbaty, M. L.; Sansone, M.; Kwiatek, P. J.; Walters, C. C.; Freund, H.; Siskin, M.; Bence, A. E.; Curry, D. J.; Solum, M.; Pugmire, R. J.; Vandenbroucke, M.; Leblond, M.; Behar, F. Direct Characterization of Kerogen by X-ray and Solid-State 13C Nuclear Magnetic Resonance Methods. *Energy Fuels* **2007**, *21*, 1548−1561.

(11) Bernard, S.; Horsfield, B.; Schulz, H.-M.; Wirth, R.; Schreiber, A.; Sherwood, N. Geochemical Evolution of Organic-Rich Shales with Increasing Maturity: A STXM and TEM Study of the Posidonia Shale (Lower Toarcian, Northern Germany). *Mar. Pet. Geol.* **2012**, *31*, 70−89. Insights into Shale Gas Exploration and Exploitation.

(12) Middleton, R. S.; Carey, J. W.; Currier, R. P.; Hyman, J. D.; Kang, Q.; Karra, S.; Jiménez-Martínez, J.; Porter, M. L.; Viswanathan, H. S. Shale Gas and Non-Aqueous Fracturing Fluids: Opportunities and Challenges for Supercritical CO_2. *Appl. Energy* **2015**, *147*, 500−509.

(13) Kim, T. H.; Cho, J.; Lee, K. S. Evaluation of CO_2 Injection in Shale Gas Reservoirs with Multi-Component Transport and Geomechanical Effects. *Appl. Energy* **2017**, *190*, 1195−1206.

(14) Omari, A.; Wang, C.; Li, Y.; Xu, X. The Progress of Enhanced Gas Recovery (EGR) in Shale Gas Reservoirs: A Review of Theory, Experiments, and Simulations. *J. Pet. Sci. Eng.* **2022**, *213*, 110461.

(15) Suleimenova, A.; Bake, K. D.; Ozkan, A.; Valenza, J. J.; Kleinberg, R. L.; Burnham, A. K.; Ferralis, N.; Pomerantz, A. E. Acid Demineralization with Critical Point Drying: A Method for Kerogen Isolation That Preserves Microstructure. *Fuel* **2014**, *135*, 492−497.

(16) Bousige, C.; Ghimbeu, C. M.; Vix-Guterl, C.; Pomerantz, A. E.; Suleimenova, A.; Vaughan, G.; Garbarino, G.; Feygenson, M.; Wildgruber, C.; Ulm, F.-J.; Pellenq, R. J. M.; Coasne, B. Realistic Molecular Model of Kerogen's Nanostructure. *Nat. Mater.* **2016**, *15*, 576−582.

(17) Van Krevelen, D. W.*Coal 3rd Edition: Typology - Physics - Chemistry - Constitution*; Elsevier, 1993.

(18) Ungerer, P.; Collell, J.; Yiannourakou, M. Molecular Modeling of the Volumetric and Thermodynamic Properties of Kerogen: Influence of Organic Type and Maturity. *Energy Fuels* **2015**, *29*, 91−105.

(19) Kashinath, A.; Szulczewski, M.; Dogru, A. H. Modeling the Effect of Maturity on the Elastic Moduli of Kerogen Using Atomistic Simulations. *Energy Fuels* **2020**, *34*, 1378−1385.

(20) Wang, T.; Tian, S.; Li, G.; Zhang, L.; Sheng, M.; Ren, W. Molecular Simulation of Gas Adsorption in Shale Nanopores: A Critical Review. *Renewable Sustainable Energy Rev.* **2021**, *149*, 111391.

(21) Collell, J.; Galliero, G.; Vermorel, R.; Ungerer, P.; Yiannourakou, M.; Montel, F.; Pujol, M. Transport of Multicomponent Hydrocarbon Mixtures in Shale Organic Matter by Molecular Simulations. *J. Phys. Chem. C* **2015**, *119*, 22587−22595.

(22) Obliger, A.; Pellenq, R.; Ulm, F.-J.; Coasne, B. Free Volume Theory of Hydrocarbon Mixture Transport in Nanoporous Materials. *J. Phys. Chem. Lett.* **2016**, *7*, 3712−3717.
(23) Béhar, F.; Vandenbroucke, M. Chemical Modelling of Kerogens. *Org. Geochem.* **1987**, *11*, 15−24.
(24) Vandenbroucke, M.; Largeau, C. Kerogen: from Types to Models of Chemical Structure. *Oil Gas Sci. Technol.* **2003**, *58*, 719−833.
(25) Siskin, M.; Scouten, C.; Rose, K.; Aczel, T.; Colgrove, S.; Pabst, R., Jr.*Composition, Geochemistry and Conversion of Oil Shales*; Snape, C., Ed.; Kluwer Academic Publishers: Dordrecht, 1995; pp 143−158.
(26) Atmani, L.; Bichara, C.; Pellenq, R. J.-M.; Van Damme, H.; van Duin, A. C. T.; Raza, Z.; Truflandier, L. A.; Obliger, A.; Kralert, P.; Ulm, F. J.; Leyssale, J.-M. From Cellulose to Kerogen: Molecular Simulation of a Geological Process. *Chem. Sci.* **2017**, *8*, 8325−8335.
(27) Zhang, T.; Li, X.; Qiao, X.; Zheng, M.; Guo, L.; Song, W.; Lin, W. Initial Mechanisms for an Overall Behavior of Lignin Pyrolysis through Large-Scale ReaxFF Molecular Dynamics Simulations. *Energy Fuels* **2016**, *30*, 3140−3150.
(28) Zheng, M.; Wang, Z.; Li, X.; Qiao, X.; Song, W.; Guo, L. Initial Reaction Mechanisms of Cellulose Pyrolysis Revealed by ReaxFF Molecular Dynamics. *Fuel* **2016**, *177*, 130−141.
(29) Zhang, T.; Li, X.; Guo, L. Initial Reactivity of Linkages and Monomer Rings in Lignin Pyrolysis Revealed by ReaxFF Molecular Dynamics. *Langmuir* **2017**, *33*, 11646−11657.
(30) Rismiller, S. C.; Groves, M. M.; Meng, M.; Dong, Y.; Lin, J. Water Assisted Liquefaction of Lignocellulose Biomass by ReaxFF Based Molecular Dynamic Simulations. *Fuel* **2018**, *215*, 835−843.
(31) Salmon, E.; van Duin, A. C.; Lorant, F.; Marquaire, P.-M.; Goddard, W. A., III Early Maturation Processes in Coal. Part 2: Reactive Dynamics Simulations Using the ReaxFF Reactive Force Field on Morwell Brown Coal Structures. *Org. Geochem.* **2009**, *40*, 1195−1209.
(32) Zhan, J.-H.; Wu, R.; Liu, X.; Gao, S.; Xu, G. Preliminary Understanding of initial Reaction Process for Subbituminous Coal Pyrolysis with Molecular Dynamics Simulation. *Fuel* **2014**, *134*, 283−292.
(33) Castro-Marcano, F.; Russo, M. F.; van Duin, A. C.; Mathews, J. P. Pyrolysis of a Large-Scale Molecular Model for Illinois no. 6 Coal Using the ReaxFF Reactive Force Field. *J. Anal. Appl. Pyrolysis* **2014**, *109*, 79−89.
(34) Zheng, M.; Li, X.; Nie, F.; Guo, L. Investigation of Overall Pyrolysis Stages for Liulin Bituminous Coal by Large-Scale ReaxFF Molecular Dynamics. *Energy Fuels* **2017**, *31*, 3675−3683.
(35) Gao, M.; Li, X.; Guo, L. Pyrolysis Simulations of Fugu Coal by Large-Scale ReaxFF Molecular Dynamics. *Fuel Process. Technol.* **2018**, *178*, 197−205.
(36) Liu, X.; Zhan, J.-H.; Lai, D.; Liu, X.; Zhang, Z.; Xu, G. Initial Pyrolysis Mechanism of Oil Shale Kerogen with Reactive Molecular Dynamics Simulations. *Energy Fuels* **2015**, *29*, 2987−2997.
(37) Pawar, G.; Meakin, P.; Huang, H. Reactive Molecular Dynamics Simulation of Kerogen Thermal Maturation and Cross-Linking Pathways. *Energy Fuels* **2017**, *31*, 11601−11614.
(38) Atmani, L.; Valdenaire, P.-L.; Pellenq, R. J.-M.; Bichara, C.; Van Damme, H.; van Duin, A. C. T.; Ulm, F. J.; Leyssale, J.-M. Simulating the Geological Fate of Terrestrial Organic Matter: Lignin vs Cellulose. *Energy Fuels* **2020**, *34*, 1537−1547.
(39) Crestini, C.; Melone, F.; Sette, M.; Saladino, R. Milled Wood Lignin: A Linear Oligomer. *Biomacromolecules* **2011**, *12*, 3928−3935.
(40) Sugita, Y.; Okamoto, Y. Replica-Exchange Molecular Dynamics Method for Protein Folding. *Chem. Phys. Lett.* **1999**, *314*, 141−151.
(41) Earl, D. J.; Deem, M. W. Parallel Tempering: Theory, Applications, and New Perspectives. *Phys. Chem. Chem. Phys* **2005**, *7*, 3910−3916.
(42) Leyssale, J.-M.; Galvez, M. E.; Valdenaire, P.-L.; Pellenq, R.; van Duin, A. C. Atomic-Scale Mechanism of Carbon Nucleation from a Deep Crustal Fluid by Replica Exchange Reactive Molecular Dynamics Simulation. *Geochim. Cosmochim. Acta* **2022**, *329*, 106−118.
(43) van Duin, A. C. T.; Dasgupta, S.; Lorant, F.; Goddard, W. ReaxFF: A Reactive Force Field for Hydrocarbons. *J. Phys. Chem. A* **2001**, *105*, 9396−9409.
(44) Srinivasan, S. G.; Ganesh, P.; van Duin, A. C. T. Development of a ReaxFF Potential for Carbon Condensed Phases and Its Application to the Thermal Fragmentation of a Large Fullerene. *J. Phys. Chem. A* **2015**, *119*, 571−580.
(45) Shin, Y. K.; Gai, L.; Raman, S.; van Duin, A. C. T. Development of a ReaxFF Reactive Force Field for the Pt-Ni Alloy Catalyst. *J. Phys. Chem. A* **2016**, *120*, 8044−8055.
(46) Valdenaire, P.-L.; Pellenq, R. J.-M.; Ulm, F. J.; van Duin, A. C. T.; Leyssale, J.-M. Timescale Prediction of Complex Multi-Barrier Pathways Using Flux Sampling Molecular Dynamics and 1D Kinetic Integration: Application to Cellulose Dehydration. *J. Chem. Phys.* **2020**, *152*, 024123.
(47) Plimpton, S. Fast Parallel Algorithms for Short-Range Molecular Dynamics. *J. Comput. Phys.* **1995**, *117*, 1−19.
(48) Swope, W. C.; Andersen, H. C.; Berens, P. H.; Wilson, K. R. A Computer Simulation Method for the Calculation of Equilibrium Constants for the Formation of Physical Clusters of Molecules: Application to Small Water Clusters. *J. Chem. Phys.* **1982**, *76*, 637−649.
(49) Shinoda, W.; Shiga, M.; Mikami, M. Rapid Estimation of Elastic Constants by Molecular Dynamics Simulation Under Constant Stress. *Phys. Rev. B* **2004**, *69*, No. 134103.
(50) Zheng, M.; Li, X.; Liu, J.; Wang, Z.; Gong, X.; Guo, L.; Song, W. Pyrolysis of Liulin Coal Simulated by GPU-Based ReaxFF MD with Cheminformatics Analysis. *Energy Fuels* **2014**, *28*, 522−534.
(51) Franzblau, D. S. Computation of Ring Statistics for Network Models of Solids. *Phys. Rev. B* **1991**, *44*, 4925−30.
(52) Debyer, Freely Available Diffraction Software. https://github.com/wojdyr/debyer.
(53) Obliger, A.; Valdenaire, P.-L.; Capit, N.; Ulm, F. J.; Pellenq, R. J.-M.; Leyssale, J.-M. Poroelasticity of Methane-Loaded Mature and Immature Kerogen from Molecular Simulations. *Langmuir* **2018**, *34*, 13766−13780.
(54) Obliger, A.; Valdenaire, P.-L.; Ulm, F.-J.; Pellenq, R. J.-M.; Leyssale, J.-M. Methane Diffusion in a Flexible Kerogen Matrix. *J. Phys. Chem. B* **2019**, *123*, 5635−5640.
(55) Monfared, S.; Zhou, T.; Andrade, J. E.; Ioannidou, K.; Radjaï, F.; Ulm, F.-J.; Pellenq, R. J.-M. Effect of Confinement on Capillary Phase Transition in Granular Aggregates. *Phys. Rev. Lett.* **2020**, *125*, No. 255501.
(56) Qu, T.; Guo, W.; Shen, L.; Xiao, J.; K, Z. Experimental Study of Biomass Pyrolysis Based on Three Major Components: Hemicellulose, Cellulose, and Lignin. *Ind. Eng. Chem. Res.* **2011**, *50*, 10424−10433.
(57) Muley, P. D.; Henkel, C.; Abdollahi, K. K.; Marculescu, C.; Boldor, D. A Critical Comparison of Pyrolysis of Cellulose, Lignin, and Pine Sawdust Using an Induction Heating Reactor. *Energy Convers. Manag.* **2016**, *117*, 273−280.
(58) Monthioux, M.; Landais, P.; Monin, J.-C. Comparison Between Natural and Artificial Maturation Series of Humic Coals from the Mahakam Delta, Indonesia. *Org. Geochem.* **1985**, *8*, 275−292.
(59) Los, J. H.; Pineau, N.; Chevrot, G.; Vignoles, G.; Leyssale, J.-M. Formation of Multiwall Fullerenes from Nanodiamonds Studied by Atomistic Simulations. *Phys. Rev. B* **2009**, *80*, No. 155420.
(60) Huang, P. Y.; Ruiz-Vargas, C. S.; van der Zande, A. M.; Whitney, W. S.; Levendorf, M. P.; Kevek, J. W.; Garg, S.; Alden, J. S.; Hustedt, C. J.; Zhu, Y.; Park, J.; McEuen, P. L.; Muller, D. A. Grains and Grain Boundaries in Single-Layer Graphene Atomic Patchwork Quilts. *Nature* **2011**, *469*, 389−392.
(61) Gamboa, A.; Farbos, B.; Aurel, P.; Vignoles, G. L.; Leyssale, J.-M. Mechanism of Strength Reduction Along the Graphenization Pathway. *Sci. Adv.* **2015**, *1*, No. e1501009.
(62) Li, Z.; Lu, C.; Xia, Z.; Zhou, Y.; Luo, Z. X-ray Diffraction Patterns of Graphite and Turbostratic Carbon. *Carbon* **2007**, *45*, 1686−1695.

https://doi.org/10.1021/acs.energyfuels.2c02963
Energy Fuels 2022, 36, 14723−14733

(63) Bernard, S.; Beyssac, O.; Benzerara, K.; Findling, N.; Tzvetkov, G.; Brown, G. XANES, Raman and XRD study of anthracene-based cokes and saccharose-based chars submitted to high-temperature pyrolysis. *Carbon* **2010**, *48*, 2506−2516.
(64) Jain, S. K.; Pellenq, R. J.-M.; Pikunic, J. P.; Gubbins, K. E. Molecular Modeling of Porous Carbons Using the Hybrid Reverse Monte Carlo Method. *Langmuir* **2006**, *22*, 9942−9948.
(65) Rouquerol, J.; Avnir, D.; Fairbridge, C. W.; Everett, D. H.; Haynes, J. M.; Pernicone, N.; Ramsay, J. D. F.; Sing, K. S. W.; Unger, K. K. Recommendations for the Characterization of Porous Solids (Technical Report). *Pure Appl. Chem.* **1994**, *66*, 1739−1758.
(66) Obliger, A.; Ulm, F.-J.; Pellenq, R. Impact of Nanoporosity on Hydrocarbon Transport in Shales' Organic Matter. *Nano Lett.* **2018**, *18*, 832−837.
(67) Helgeson, H. C.; Richard, L.; McKenzie, W. F.; Norton, D. L.; Schmitt, A. A Chemical and Thermodynamic Model of Oil Generation in Hydrocarbon Source Rocks. *Geochim. Cosmochim. Acta* **2009**, *73*, 594−695.

https://doi.org/10.1021/acs.energyfuels.2c02963
Energy Fuels 2022, 36, 14723−14733